Journal of Materials Chemistry A

ROYAL SOCIETY OF CHEMISTRY

PAPER

View Article Online
View Journal

Cite this: DOI: 10.1039/d5ta03813h

Coupled influence of state-of-charge and storage temperature on calendar aging and subsequent cycle degradation in $LiFePO_4$/graphite pouch cells†

Wenjun Shen,[ab] Jinyang Dong,*[ab] Yun Lu,[ab] Kang Yan,[b] Yibiao Guan,*[c] Guangjin Zhao,[d] Bowen Li,[d] Xi Wang,[ab] Rui Tang,[ab] Jialong Zhou,[ab] Ning Li,[ab] Yuefeng Su,*[ab] Feng Wu[ab] and Lai Chen *[ab]

Understanding the full-lifecycle degradation behavior of lithium-ion batteries requires simultaneous attention to calendar aging and cycle aging, which differ in mechanisms but are inherently interconnected. This study systematically investigates how high-temperature storage under different state-of-charge (SOC) conditions influences subsequent cycling performance in $LiFePO_4$/graphite pouch cells. Under 55 °C storage, batteries aged at high SOC exhibit more severe capacity fade, lithium inventory loss, and interfacial degradation compared to those stored at lower SOC. Multi-scale and multi-dimensional analyses reveal that calendar aging at elevated SOC accelerates side reactions, promotes SEI thickening, induces interfacial inhomogeneity, and triggers structural disorder. These chemical and mechanical deteriorations do not terminate with storage but persist and evolve under subsequent cycling, leading to increased resistance, reduced phase reversibility, and long-term performance decline. In contrast, low-SOC storage preserves structural and interfacial stability, enabling better cycling durability. The findings demonstrate that calendar aging functions as a critical precursor that shapes the trajectory and severity of ensuing cycle aging. Aging behavior in storage stages sets the foundation for electrochemical failure under dynamic conditions. This study highlights the need to address both aging types within an integrated framework, offering mechanistic insights for predictive modeling and practical guidance for optimizing storage and usage protocols in electric vehicle and stationary energy storage systems.

Received 12th May 2025
Accepted 9th July 2025

DOI: 10.1039/d5ta03813h

rsc.li/materials-a

[a]School of Materials Science and Engineering, Beijing Key Laboratory of Environmental Science and Engineering, Beijing Institute of Technology, Beijing 100081, China. E-mail: chenlai144@sina.com

[b]Chongqing Innovation Center, Beijing Institute of Technology, Chongqing 401120, China

[c]China Electric Power Research Institute, Beijing 100192, China

[d]State Grid Henan Electric Power Research Institute, Zhengzhou 450052, China

† Electronic supplementary information (ESI) available. See DOI: https://doi.org/10.1039/d5ta03813h

Lai Chen

Lai Chen is a Distinguished Research Fellow and PhD supervisor at the School of Materials Science and Engineering, Beijing Institute of Technology, and Deputy Director of the Beijing Institute of Technology Chongqing Innovation Center. He was selected for the 4th Youth Talent Support Program of the China Association for Science and Technology and the Beijing Nova Program. He has led over ten projects as principal investigator, including the National Key R&D Program of China, the National Natural Science Foundation of China, and the Yibin 'Jie Bang Gua Shuai' Project. He has also participated in major initiatives such as the National Basic Research Program of China (973 Program) and the National Key R&D Program on New Energy Vehicles. Since 2013, he has published over 60 SCI papers including Advanced Materials, Advanced Energy Materials, and Materials Today, holds 32 granted patents, and authored three academic books. His research focuses on lithium-ion and other electrochemical energy storage systems, particularly lithium-rich cathode materials, nickel-rich cathodes, and high-energy-density batteries.

Introduction

Lithium-ion batteries (LIBs), especially the lithium iron phosphate/graphite (LFP/Gr) system, have been widely applied in portable electronic devices and electric vehicles due to their advantages such as high energy density, safety and cost-effectiveness.[1] However, both during usage and storage, their performance is significantly affected by battery aging mechanisms, which in turn play a crucial role in the long-term performance of the batteries.[2,3] Two major forms of battery aging—cycle aging and calendar aging—are central to understanding and improving battery lifespan. Cycle aging refers to degradation caused by repeated charging and discharging, while calendar aging arises when the battery is stored at rest without cycling. Historically, research has focused more on cycle aging, given its direct link to daily battery operation.[4,5] Nonetheless, as LIBs are increasingly used in systems that experience long idle periods, such as electric vehicles or backup power systems, calendar aging has become equally critical. Cycle aging is driven by mechanical and electrochemical stresses during lithium insertion and extraction. Repeated changes in the state of charge (SOC) induce expansion and contraction in active materials, leading to particle cracking, electrode delamination, and loss of electrical contact.[6–8] These effects accelerate at high SOC and aggressive current rates. To solve these problems, strategies like narrowing the SOC window, optimizing charging protocols, and modifying electrode microstructures have been applied to minimize structural fatigue and maintain performance.[9,10] In contrast, calendar aging occurs in the absence of cycling and is dominated by chemical side reactions at the electrode–electrolyte interfaces.[11–13] Key mechanisms include the growth of the solid electrolyte interphase (SEI) on the anode, cathode–electrolyte reactions, and continuous electrolyte decomposition.[14,15] These processes lead to lithium loss, impedance rise, and capacity fade. Calendar aging is strongly dependent on temperature and SOC, with higher values accelerating degradation. Under actual operating conditions, clarifying different types of aging and their degrees of influence is important for building battery life prediction models and optimizing storage strategies.[16] For application scenarios that require both rapid charging and long standby times, it is crucial to comprehensively consider all aspects of battery aging.

While calendar and cycle aging both contribute to the long-term degradation of lithium-ion batteries, their mechanisms, influencing factors, and operational implications are basically different. Cycle aging is largely controlled by repetitive lithiation and delithiation processes, which induce structural and mechanical damage in the electrode materials.[17,18] This includes phase transitions, volumetric strain, and particle fracture, especially under wide SOC windows and high charge/discharge rates. The resulting structural fatigue leads to active material isolation, reduced conductivity, and capacity decline over time.[19,20] Consequently, extensive efforts have been devoted to optimizing cycling parameters and material design to alleviate cycle-induced degradation. In contrast, even if the battery is idle, calendar aging will still continue to occur. This process is mainly driven by the chemical and electrochemical instability under high temperature or high SOC.[21] These conditions enhance the reactivity of electrode surfaces with the electrolyte, leading to parasitic side reactions, SEI or CEI layer thickening, and lithium inventory loss.[22,23] Unlike the cyclic aging dominated by mechanical fatigue, the characteristic of calendar aging lies in the continuous interface degradation.[24,25] Even in the absence of volume stress, this degradation will occur. Experimental studies, such as those by Kassem and Stroe, have demonstrated that batteries stored at high SOC and elevated temperatures experience accelerated capacity fade and impedance growth, highlighting the critical role of storage conditions. Moreover, recent findings indicate that the two aging modes are not isolated.[26,27] Degradation initiated during calendar aging, such as SEI instability or passive film growth, may predispose electrodes to increased damage during subsequent cycling. Similarly, the effects of cycling can alter the chemical environment of electrode surfaces, influencing their behavior during storage.[28–30] This interdependent relationship indicates that evaluating battery lifespan requires a comprehensive consideration of aging models during both the idle and usage phases.[31,32] Most existing studies have focused on individual aspects such as the effects of temperature, state-of-charge, or storage duration on capacity decay. These works have elucidated specific degradation mechanisms—for instance, the evolution of the solid electrolyte interphase, lithium inventory loss, and the influence of storage conditions on battery stability. In practical application scenarios such as electric vehicles or grid energy storage, where intermittent operation exists, if the interaction between calendar aging and cycle aging is not taken into account, the degree of battery degradation may be underestimated, leading to an imperfect system design. Therefore, understanding the correlation between these two aging modes is crucial for formulating effective management strategies to extend battery life.

This study investigates the effect of calendar aging conditions on the subsequent cycling performance of $LiFePO_4$/graphite (LFP–C) pouch cells, with particular emphasis on the influence of storage temperature and state of charge (SOC). Initial analysis reveals that prolonged storage at elevated temperatures and high SOC leads to pronounced capacity loss, largely attributed to progressive side reactions at the electrode–electrolyte interfaces. These reactions result in the accumulation of degradation products, thickening of interfacial layers, and partial consumption of active lithium, even in the absence of external cycling. Notably, elevated temperatures accelerate these parasitic processes, while high SOC enhances the reactivity of electrode surfaces, thereby exacerbating interfacial instability. Building on the calendar aging phase, the study further evaluates how these pre-storage conditions impact the batteries' response to subsequent cycling. The results demonstrate that cells subjected to harsher storage conditions exhibit reduced cycle life, lower coulombic efficiency, and increased resistance accumulation during cycling. These effects are closely related to the preformed interfacial degradation and structural weakening induced during storage, which impair the electrodes' ability to accommodate

repeated lithium insertion and extraction. The findings highlight a strong coupling between storage-induced chemical degradation and later mechanical and electrochemical failure. This work underscores the necessity of considering calendar aging not as an isolated phenomenon but as a preconditioning stage that critically influences long-term cycling stability. Such insights are essential for developing predictive aging models and informing practical storage and usage protocols in real-world energy systems.

Results and discussion

Battery capacity degradation

To elucidate the degradation mechanisms associated with calendar aging, we conducted a one-year high-temperature storage experiment on $LiFePO_4$/graphite (LFP–C) pouch cells maintained at 55 °C under two state-of-charge (SOC) conditions: 50% and 75%, denoted as 50SOC-CA and 75SOC-CA. The objective was to investigate how storage SOC influences capacity retention and internal resistance evolution. As shown in Fig. 1a, capacity gradually decreased in both cases, with the 75SOC-CA cells exhibiting a significantly faster decline, indicating that higher SOC accelerates degradation during calendar aging. To further understand the electrochemical kinetics during storage, electrochemical impedance spectroscopy (EIS) was employed to characterize resistance buildup and ion transport dynamics. The resulting Nyquist plots (Fig. 1b and e) demonstrate that impedance increased progressively over time, reflecting the accumulation of interfacial resistance and deterioration of electrode–electrolyte contact. To deconvolute overlapping impedance contributions and clarify the nature of resistive processes, we applied the distribution of relaxation times (DRT) analysis.[33] The aim of this analysis was to resolve time-resolved electrochemical processes and distinguish bulk conduction, interphase evolution, and charge transfer. As illustrated in Fig. 1c, d, f and g, three characteristic peaks emerged: F1 (bulk conduction), F2 (interfacial processes such as SEI/CEI formation), and F3 (charge transfer). Among these, the F2 peak—primarily associated with SEI growth on the graphite anode—exhibited the most dynamic evolution. Fig. 1 further shows that F2 first increased with aging time and then slightly declined, indicating that the SEI initially thickens and subsequently undergoes partial reorganization or degradation. This trend was more pronounced and initiated earlier in the 75SOC-CA cell, suggesting that high SOC not only accelerates SEI formation but may also destabilize the interphase structure over time. These results highlight that storage-induced electrochemical environments, especially SOC, profoundly influence interfacial evolution and resistance accumulation during calendar aging.

Degradation mechanisms investigated by disassembly and characterization

To study the influence of the individual electrodes on the battery's storage performance, we analyzed both the cathode and

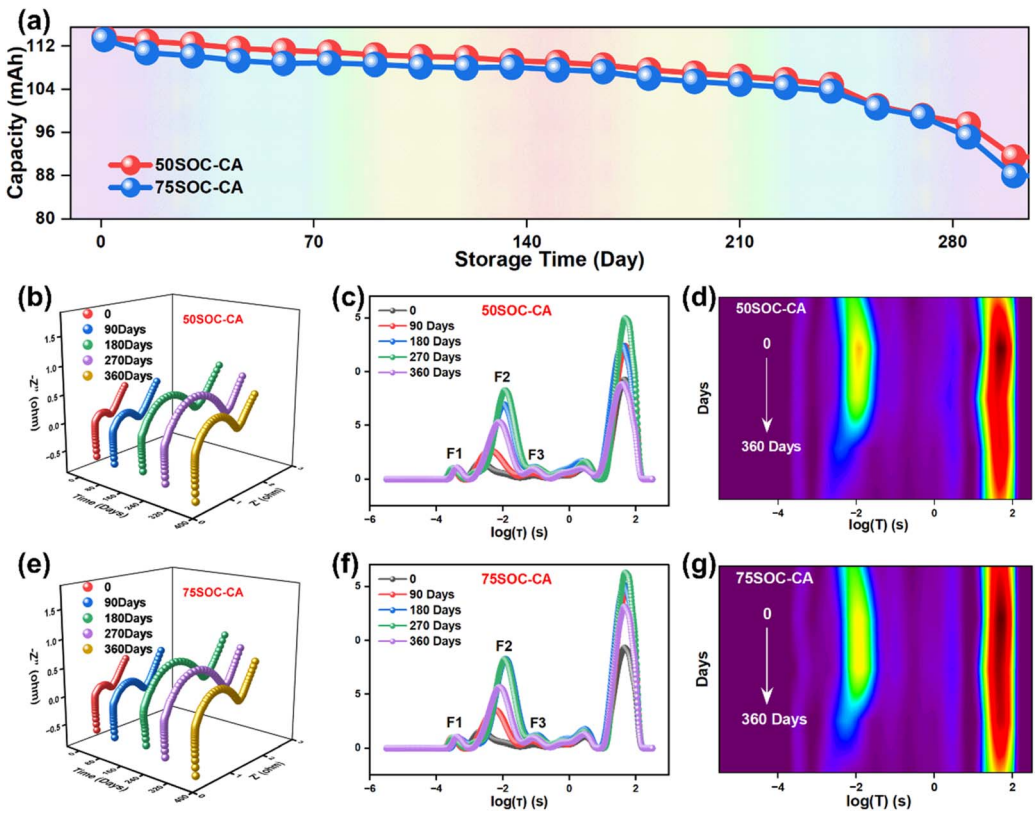

Fig. 1 (a) Discharge capacities measured at 55 °C for the cells under different storage conditions of SOC. Static EIS test results of impedance at different SOCs (b and e), with (c, f, d and g) corresponding DRT plots.

anode extracted from full cells after storage, which were denoted as 50SOC-PE-CA and 75SOC-PE-CA, corresponding to storage at 50% and 75% state of charge, respectively. To evaluate structural changes in electrode materials after long-term high-temperature storage, scanning electron microscopy (SEM) was conducted on LFP/graphite pouch cells stored at 55 °C under different state-of-charge (SOC) conditions. Fig. 2(a and b) show the surface morphology of cathode materials aged at 50% and 75% SOC. At 50SOC-PE-CA, the $LiFePO_4$ particles retain their original morphology with no significant cracks or deformation. In contrast, at 75SOC-PE-CA, visible surface cracking and particle fracture are observed, particularly at higher magnification, indicating deterioration in particle cohesion and connectivity. The presence of microcracks on the LFP surface suggests structural weakening, which may contribute to increased resistance and hinder lithium-ion diffusion within the electrode. SEM images of the anode surface, shown in Fig. 2(c and d), reveal a progressive increase in surface roughness and particle damage with rising SOC. At 50SOC-PE-CA, the graphite layers exhibit slight exfoliation, and fine deposits begin to accumulate on the particle surface, consistent with initial formation of the solid electrolyte interphase (SEI). As the SOC increases to 75%, more severe degradation is evident: active particles show significant fracture and fragmentation, and the entire surface becomes covered by thick, uneven passivation films. The accumulation of these films, likely originating from electrolyte reduction, is accompanied by an increase in surface inhomogeneity and porosity. The high-SOC samples also exhibit substantial buildup of interfacial layers and localized loss of structural integrity, indicating that elevated SOC accelerates chemical reactions at the electrode–electrolyte interface. The observed cracking and surface film formation suggest that side reactions intensify with SOC, leading to more extensive SEI growth and deposition of decomposition products. The results demonstrate that SOC significantly influences the extent of electrode morphological degradation during calendar aging.

In addition, to further isolate the intrinsic storage behavior of each electrode, the positive and negative electrodes were stored independently under identical conditions, and referred to as 50SOC-SPE-CA and 75SOC-SPE-CA. X-ray diffraction (XRD) analysis was conducted to evaluate the structural evolution of

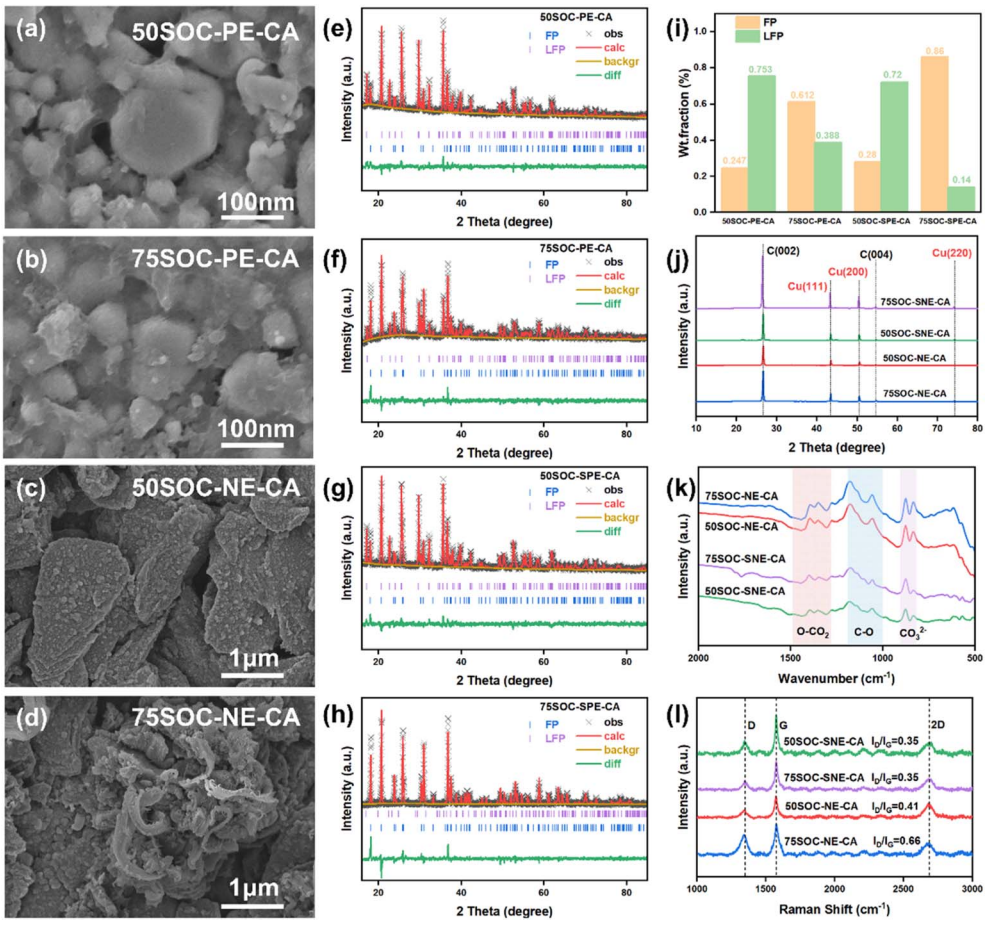

Fig. 2 Morphological changes and surface composition analysis of the electrode after calendar aging. SEM image of (a) 50SOC-PE-CA, (b) 75SOC-PE-CA, (c) 50SOC-NE-CA, (d) 75SOC-NE-CA. XRD Rietveld refinement results of positive electrode from (e) 50SOC-PE-CA, (f) 75SOC-PE-CA, (g) 50SOC-SPE-CA, (h) 75SOC-SPE-CA. (i) XRD Rietveld refinement results of proportion of LFP and FP. (j) XRD patterns of negative electrodes at different storage conditions. (k) FT-IR spectra of negative electrodes at different storage conditions. (l) Raman spectra of negative electrodes at different storage conditions.

$LiFePO_4$/graphite electrodes following long-term storage under varying state-of-charge (SOC) conditions. As shown in the XRD patterns of the aged cathodes, $LiFePO_4$ retains its characteristic olivine-type structure across all storage conditions, indicating that the bulk phase remains stable during calendar aging. However, a clear increase in the intensity of diffraction peaks associated with the $FePO_4$ phase is observed as SOC increases. This enhancement suggests partial delithiation of $LiFePO_4$ and implies a loss of reversible lithium from the host structure during storage, particularly under high SOC conditions.[34,35] The formation of $FePO_4$ in discharged electrodes indicates that lithium ions are consumed in side reactions and become electrochemically inactive. These results point to a gradual reduction in active lithium inventory, which may impact long-term capacity retention. The key XRD Rietveld refinement parameters are shown in Table S1.† To further examine whether structural changes occurred in the negative electrode, XRD patterns of aged graphite anodes were compared with those of fresh samples. As illustrated in Fig. 2j, the diffraction peak positions remain consistent across all conditions, with no peak broadening, disappearance, or emergence of new reflections. This indicates that the crystalline structure of graphite remains intact regardless of SOC during storage. Despite signs of Cu current collector corrosion observed through other characterization methods, the core graphite phase appears structurally preserved. Similarly, for the positive electrode, peak positions remain stable, with no evidence of peak shifting, loss, or formation of secondary phases, confirming the structural integrity of the $LiFePO_4$ framework throughout the aging process. These findings collectively demonstrate that while the electrode materials maintain their bulk crystal structures after calendar aging, SOC influences the extent of lithium deintercalation and alters the electrochemical reversibility of the cathode, potentially affecting subsequent cycling performance.

To further elucidate the chemical and structural evolution of the interfacial layer on the graphite anode during storage, Fourier Transform Infrared Spectroscopy (FT-IR) was employed. As shown in the spectral data, the 75S0C-NE-CA exhibits enhanced absorption peaks corresponding to organic species such as C–O, C═O, and O–CO_2, relative to the electrode prior to storage. In contrast, the characteristic signal associated with inorganic carbonate (CO_3^{2-}) species diminishes significantly. This indicates a compositional shift within the solid electrolyte interphase (SEI), suggesting that the originally formed SEI—typically loose, porous, and rich in inorganic components—undergoes substantial reorganization during long-term aging.

The incomplete coverage of the electrode by the initial SEI leaves exposed regions susceptible to further electrolyte reduction. Over time, these reactions result in the formation of a secondary SEI layer that is thicker and increasingly dominated by organic species. The increase in organic components, which possess poorer electronic insulating properties compared to inorganic compounds, exacerbates parasitic solvent reduction reactions and promotes continued SEI growth until a critical thickness is reached. These findings provide mechanistic insight into the degradation pathway of the anode and support the hypothesis that extended storage under elevated SOC conditions facilitates the accumulation of resistive and unstable SEI products. Complementary Raman spectroscopy analysis of the aged anode, presented in Fig. 2l, shows three primary features: the D band ($\sim$1350 cm^{-1}) corresponding to disordered graphite, the G band ($\sim$1580 cm^{-1}) related to sp^2-hybridized carbon, and the 2D band ($\sim$2700 cm^{-1}) indicative of interlayer stacking. The I_D/I_G ratio, a commonly used metric for assessing defect density,[36] increases markedly with SOC and reaches a value of 0.66 at 75SOC-NE-CA, confirming significant lattice disorder and structural degradation of the graphite. Combined with XRD observations, these results confirm that high SOC storage not only alters SEI chemistry but also promotes structural breakdown of the electrode, contributing to lithium loss and performance decline.

To investigate the compositional evolution of the anode surface following prolonged storage under different state-of-charge (SOC) conditions, X-ray photoelectron spectroscopy (XPS) was employed to analyze key elements contributing to interfacial chemistry. The quantitative results are summarized in Tables S2–S5.† The C 1s spectra (Fig. 3a, e, i and m) consistently exhibit four deconvoluted peaks at binding energies of 284.8 eV (C–C/C–H), 286.3 eV (C–O), 288.8 eV (C═O), and 291.1 eV (C–F/CO_3^{2-}).[37] A systematic decline in the intensity of the CO_3^{2-}-related peak is observed with increasing SOC, suggesting that Li_2CO_3 decomposes more readily under higher SOC conditions during storage. Correspondingly, the O 1s spectra (Fig. 3b, f, j and n) display two dominant peaks assigned to CO_3^{2-} (531.8 eV) and C–O (533.8 eV), with a similar trend: the relative proportion of CO_3^{2-} diminishes as SOC increases, aligning with the C 1s findings. The F 1s spectra (Fig. 3c, g, k and o) exhibit characteristic peaks at 685.5 eV and 688.0 eV, attributable to Li–F and P–F bonds, respectively, reflecting the decomposition of $LiPF_6$. A noticeable reduction in the LiF signal at higher SOC, particularly at 75SOC-NE-CA, suggests less accumulation of LiF species under these conditions despite constant temperature. The P 2p spectra (Fig. 3d, h, l and p) reveal two peaks: one at 133.3 eV (P–O/P═O), inherent to the $LiFePO_4$ cathode, and another at 136.1 eV (P–F), indicating the presence of phosphorus–fluorine species derived from electrolyte breakdown. However, no significant variation is observed in the intensity of the P–F signal across different SOCs, implying that SOC has a minimal effect on the generation of P–F species or Li_3PO_4 content within the cathode electrolyte interphase (CEI). Overall, storage at elevated SOC results in reduced Li_2CO_3 and LiF content on the anode surface, reflecting compositional shifts in the SEI and CEI layers driven by electrolyte decomposition and interfacial reactions during long-term aging.

Structural and interfacial analyses based on XRD, Raman spectroscopy, FT-IR and XPS revealed that high state-of-charge (SOC) conditions during storage induced more significant material degradation, including increased lattice disorder and interfacial instability. Furthermore, comparison between full-cell and separately stored electrodes under the same SOC demonstrated that degradation was more severe in the full-cell configuration. These results suggest that, in addition to the intrinsic effect of SOC, direct electrochemical and chemical interactions between the cathode and anode in full-cell storage

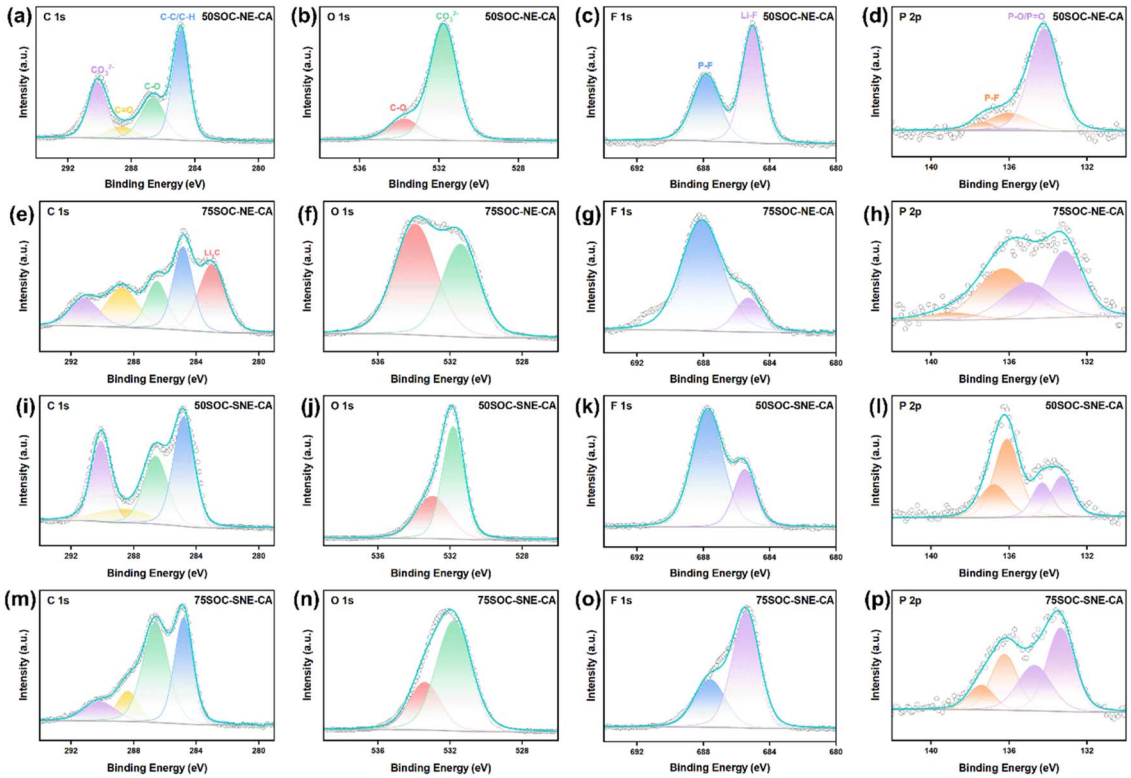

Fig. 3 XPS results of C 1s, O 1s, F 1s, and P 2p of graphite anodes after storage at (a–d) 50SOC-NE-CA, (e–h) 75SOC-NE-CA, (i–l) 50SOC-SNE-CA, and (m–p) 75SOC-SNE-CA, respectively.

further accelerate lithium loss and aggravate long-term performance decline.

Cyclic analysis

The cycling stability of $LiFePO_4$/graphite (LFP/Gr) batteries following storage under different state-of-charge (SOC) conditions demonstrates a strong dependence on temperature and prior storage history. As shown in Fig. 4a, when cycled at 55 °C, batteries stored at 50% SOC retained approximately 85% of their initial capacity after 1500 cycles, while those stored at 75% SOC maintained a similar retention of 84.8%. Despite comparable overall capacity, both groups exhibited a two-stage degradation process. The initial phase, known as the activation stage, spans the first 100 cycles and is attributed to interfacial stabilization driven by solid electrolyte interphase (SEI) layer growth, which helps passivate reactive surfaces and delay rapid capacity loss. This is followed by a linear capacity fading stage, reflecting steady long-term degradation. Incremental capacity (IC) analysis (Fig. 4d and g) further illustrates the impact of storage SOC. Both 50SOC-CY and 75SOC-CY samples show a progressive decline in Peak I intensity, while Peak II remains relatively stable, indicating that loss of active lithium (LLI) is the primary aging mechanism at this temperature, with less contribution from loss of active material (LAM). The rightward shift of Peaks I and II suggests a reduction in thermodynamic polarization and an increase in discharge voltage, reflecting changes in interfacial kinetics. Differential voltage (DV) curves (Fig. 4c and f) show narrowing profiles over time, consistent with capacity loss. At 55 °C, QI declines markedly, while QII and QIII show moderate decreases, implying that LAM becomes more pronounced as cycling continues. Batteries stored at 50SOC-CY display slightly lower polarization and a slower decrease in QII and QIII compared to those stored at 75SOC-CY, suggesting that lower SOC storage mitigates structural degradation and interfacial instability.[38,39] These results emphasize the influence of pre-cycling storage conditions on long-term performance, even under identical thermal and cycling protocols. Ultrasonic imaging was employed to non-destructively assess internal electrolyte distribution and structural uniformity after storage. As shown in Fig. 4(h and i), both the 50SOC-CY and 75SOC-CY cells exhibited high and uniform ultrasonic transmission at 55 °C, indicating no evident macroscopic delamination or electrolyte depletion.

To further investigate the impact of storage SOC on electrode interfacial properties and mechanical behavior during subsequent cycling at elevated temperatures, electrochemical impedance spectroscopy (EIS) and volume expansion measurements were conducted. EIS analysis enables resolution of individual resistive contributions related to SEI formation, charge transfer kinetics, and internal diffusion, while expansion testing provides insight into electrode swelling, which reflects cumulative structural stress during lithium-ion insertion and extraction. As illustrated in the distribution of relaxation times (DRT) plots derived from EIS spectra (Fig. 5g–n), the impedance response consists of contributions from ohmic

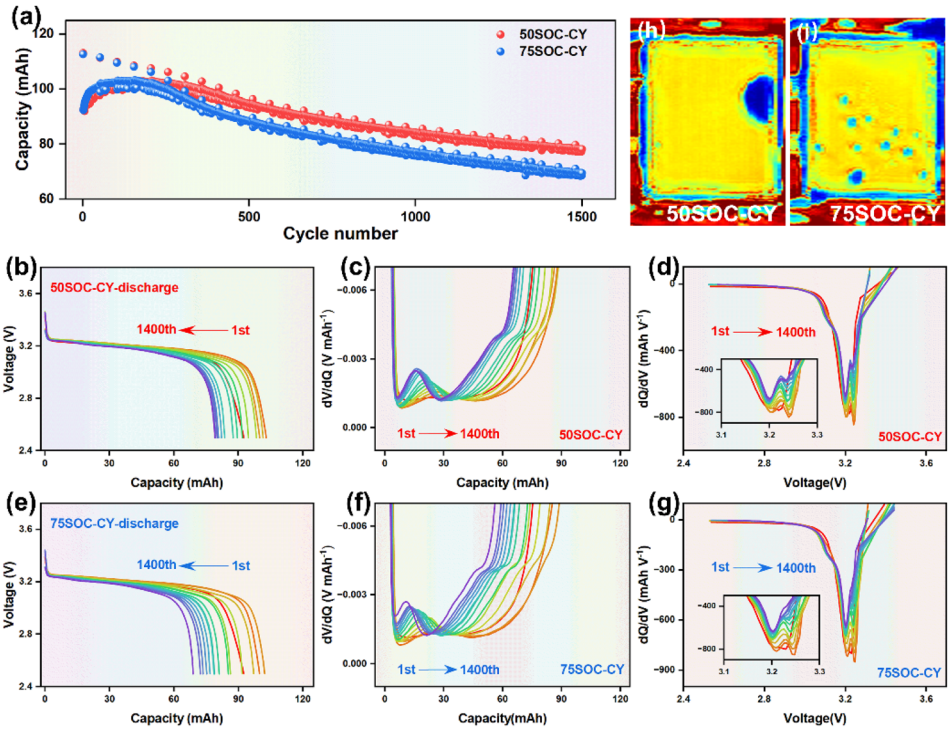

Fig. 4 Cycling stability characterization after long-term high-temperature and storage. (a) Cycling curve. The corresponding charge–discharge curves of different cycles for (b) SoC50 pouch cell and (e) SoC75 pouch cell. The corresponding d*V*/d*Q* curves for (c) SoC50 pouch cell and (f) SoC75 pouch cell. The corresponding d*Q*/d*V* curves for (d) SoC50 pouch cell and (g) SoC75 pouch cell. (h and i) Ultrasound images of the cell after cycling.

resistance, SEI film resistance, charge transfer resistance of both electrodes, and a low-frequency process related to sluggish anode dynamics. At 55 °C, the 50SOC-CY cell (Fig. 5i) exhibits lower total impedance and more defined DRT peak shapes than the 75SOC-CY cell (Fig. 5m), indicating more favorable charge transfer behavior and reduced interfacial degradation. The results suggest that lower SOC storage conditions help suppress electrolyte decomposition and SEI overgrowth, thereby preserving interfacial stability. In contrast, the higher impedance observed in the 75SOC-CY cell reflects aggravated side reactions, SEI thickening, and kinetic hindrance at the electrode–electrolyte interface. Mechanical responses during cycling were also analyzed through *in situ* volume expansion testing (Fig. 5a–f). Three distinct expansion stages were observed: an initial peak during the charging plateau (~3.4 V) associated with lithium intercalation, a maximum at full charge, and a third peak near the end of discharge, potentially linked to lithium plating or gas release. The 75SOC-CY cell exhibited more pronounced expansion in all stages, indicating higher structural strain. The DRT fitting plots from the EIS results are shown in the Fig. S10(a–d).† In Fig. S10(a and b),† a progressive increase in impedance (V(T)) is observed with rising voltage, suggesting enhanced charge-transfer resistance at the electrode–electrolyte interface. This could be attributed to phase transitions in the cathode material or oxidative side reactions at elevated potentials. In Fig. S10(c and d),† the impedance decreases with reducing voltage, implying lower kinetic barriers for Li^+ intercalation at the anode. Furthermore, there is a pronounced impedance surge at 3.7 V may indicate SEI degradation or irreversible oxidation products accumulating at the interface. And it can be observed that the battery impedance increases with higher storage SOC levels. To further quantify these effects, electrode thickness and resistivity were measured using a four-point probe electrode resistance meter (BER2500, IEST, Xiamen), as shown in Fig. S2(a and b).† While the positive electrode exhibited minimal variation, the negative electrode in the 75SOC-CY cell showed substantial thickening and resistivity rise, consistent with graphite particle disconnection, SEI accumulation, and reduced electron conduction pathways under high SOC storage.

To assess the structural degradation of cell components under different storage SOCs and elevated temperatures, post-cycling analyses of the cathode, separator, and anode were conducted through battery disassembly and imaging. As shown in Fig. S3,† optical photographs of the aged cathodes reveal evident material detachment. White regions on the electrode surface correspond to exposed aluminum current collectors, indicating loss of the active material layer. While some detachment may occur during manual disassembly, the dominant cause is attributed to diminished adhesion between the active material and current collector under thermal and electrochemical stress. This is likely driven by binder decomposition and mechanical degradation of the LFP structure.[40] At 55 °C, the 50SOC-CY cell exhibits relatively minor material loss,

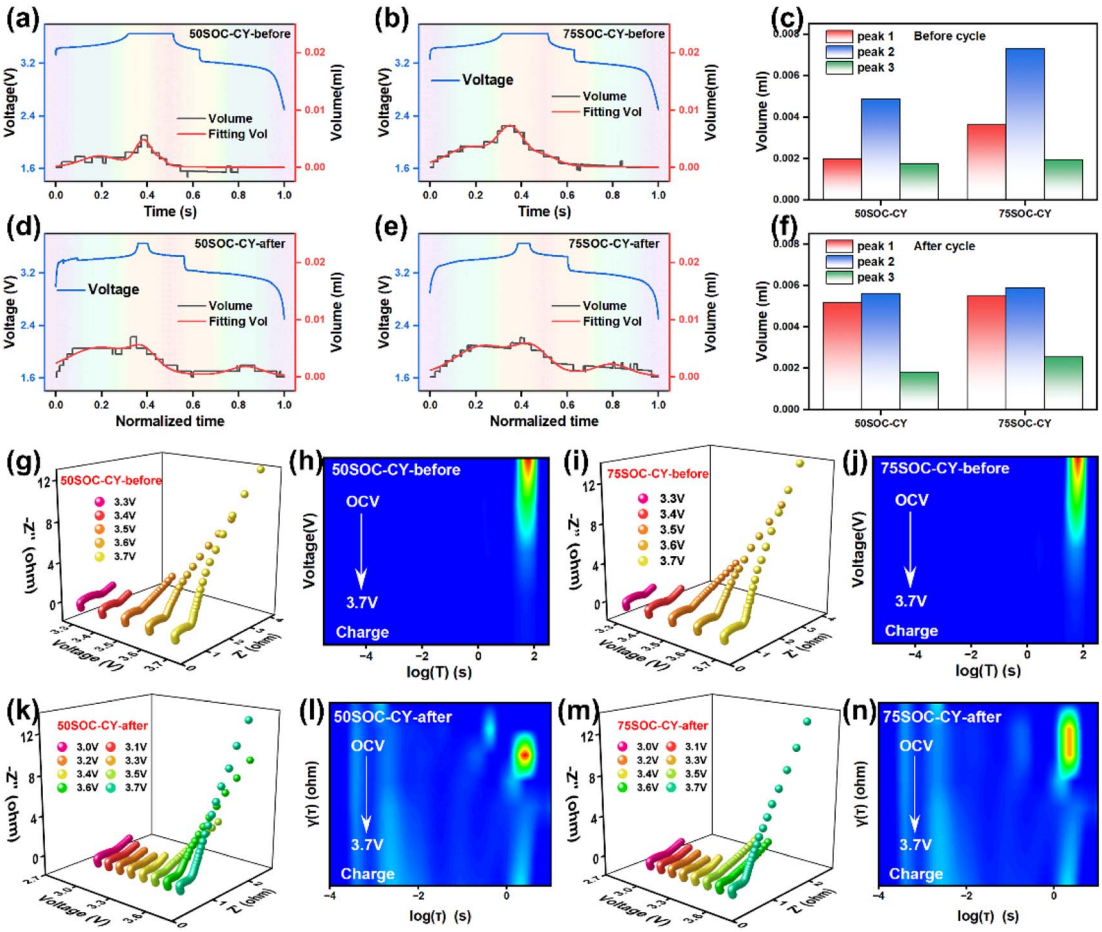

Fig. 5 Performance and structural evolution during long-term high-temperature storage. (a–f) Volume changes. *In Situ* EIS test results of impedance at different SOCs (g, i, k and m), with (h, j, l and n) corresponding DRT plots.

while the 75SOC-CY cathode shows widespread delamination and cracking, pointing to a greater extent of structural failure. The separator surface under 75SOC-CY also exhibits considerable adhesion of cathode debris, potentially blocking pores and disrupting lithium-ion transport. Scanning electron microscopy (SEM) images (Fig. S4†) further illustrate changes in cathode and anode morphology. At 55 °C, LFP particles on the cathode surface remain generally intact, though mild surface roughening is observed under high SOC conditions. In contrast, the negative electrode displays more significant degradation. As SOC increases, the graphite surface becomes increasingly covered with electrolyte decomposition products and shows greater morphological disruption. In particular, at 75SOC-CY (Fig. S4d†), fractured graphite particles and dense passivation films are evident, suggesting increased SEI formation and reduced electronic conductivity. These features indicate that higher SOC during thermal storage accelerates interfacial reactions and structural deterioration in the negative electrode. Collectively, the optical and microscopic characterizations demonstrate progressive component degradation under high SOC and elevated temperature, with clear impacts on both electrode integrity and separator contamination.

To elucidate the structural evolution of electrode materials influenced by prior storage conditions, *in situ* X-ray diffraction (XRD) analysis was performed on LFP/Gr pouch cells subjected to calendar aging at different states of charge (SOC). Powder samples were scraped from the aged cathode and anode electrodes and assembled into coin cells for *in situ* tracking of phase transitions during subsequent charge–discharge cycling. This method enables investigation of the coupling between calendar aging and cycling behavior at the material level. For the cathode, $LiFePO_4$ undergoes a two-phase transition during delithiation, forming $FePO_4$ (FP), which reverts to $LiFePO_4$ upon lithiation.[41,42] As shown in Fig. 6a and b, aged cathode materials exhibit characteristic LFP and FP coexistence throughout the charging plateau. At the cutoff voltage of 3.7 V, LFP peaks disappear, indicating complete conversion to FP; upon discharge, these peaks reappear without impurity signals, demonstrating preserved phase reversibility. Volume change analysis reveals that cathodes stored at 50SOC-CY display larger lattice fluctuations during cycling compared to 75SOC-CY, indicating more active lithium insertion and extraction kinetics, likely due to reduced passivation and less lithium depletion during prior storage. *In situ* XRD analysis of graphite anodes retrieved from aged cells shows clear staging behavior:

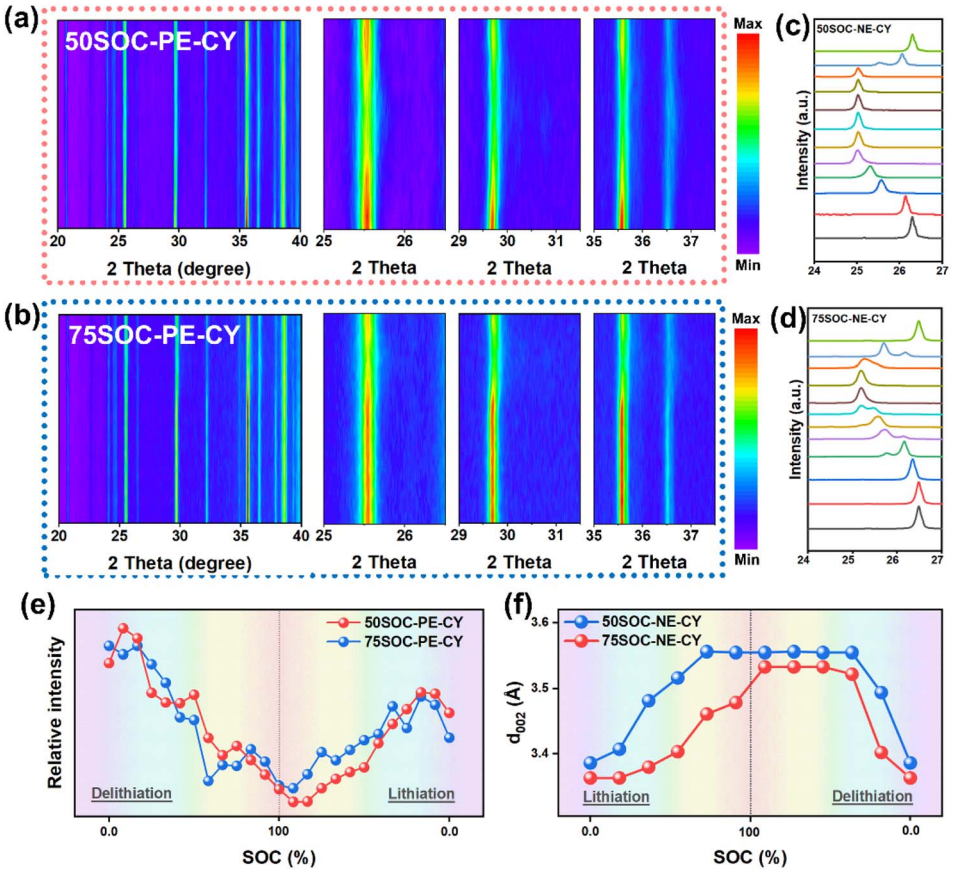

Fig. 6 Structural evolution during the initial charging process after long-term high-temperature storage. *In situ* XRD patterns of (a) 50SOC-PE-CY and (b) 75SOC-PE-CY. *In situ* XRD patterns of (c) 50SOC-NE-CY and (d) 75SOC-NE-CY. (e) The corresponding relative intensity of LFP. (f) The corresponding *d*-spacings of (003) diffraction peaks.

from pristine graphite to stage IV (0.850–0.198 V), followed by transitions to stage III (0.198–0.170 V), stage II (0.110–0.075 V), and finally stage I (0.075–0 V). Lithiation begins near 0.845 V, correlating with SEI formation onset. At 55 °C, the graphite electrode shows more pronounced changes in lattice parameters with increasing SOC, as depicted in Fig. 6f. Compared to the cathode, the anode exhibits greater structural sensitivity to SOC history. These observations demonstrate that storage-induced degradation alters subsequent phase transition behavior in both electrodes, suggesting that calendar aging exerts a measurable influence on the reversibility and structural dynamics of electrodes during later cycling stages.

To examine the structural evolution of the cathode after extended cycling following different calendar aging conditions, X-ray diffraction (XRD) and high-resolution transmission electron microscopy (HRTEM) were utilized to analyze the aged positive electrode materials stored at 50% and 75% SOC and cycled at 55 °C. XRD analysis revealed that after long-term cycling, the LFP cathode stored at 75SOC-PE-CY exhibited increased complexity in phase composition, as evidenced by additional impurity peaks and diminished $LiFePO_4$ (LFP) phase intensity. In contrast, the $FePO_4$ (FP) phase became more pronounced, as confirmed by Rietveld refinement (Fig. 7a and b). This increase in FP phase and the corresponding reduction in LFP intensity suggest that fewer lithium ions were reversibly intercalated into the $FePO_4$ lattice during cycling, likely due to lithium inventory loss (LLI) accumulated during prior storage.[43,44] Notably, despite the change in peak intensity, no discernible shift toward lower diffraction angles was observed for either LFP or FP phases in either SOC condition, indicating that the overall crystallinity and lattice symmetry were preserved and no significant amorphization occurred. Complementary HRTEM analysis (Fig. 7c and d) further revealed microstructural distinctions. The cathode aged under 75SOC-PE-CY showed prominent LFP lattice fringes alongside minor disordered domains and small regions of FP phase, indicating partial structural degradation. In contrast, the cathode stored at 50SOC-PE-CY maintained a more continuous and homogeneous LFP lattice, with limited FP formation and fewer disordered areas, reflecting relatively intact structural integrity. Additionally, geometric phase analysis (not shown here) indicated that both conditions led to comparable levels of lattice strain after prolonged cycling, suggesting that while storage SOC impacts phase composition and microstructure, the resulting internal stress distribution may remain similar. These findings suggest that higher storage SOC prior to cycling accelerates lithium depletion and phase heterogeneity in the

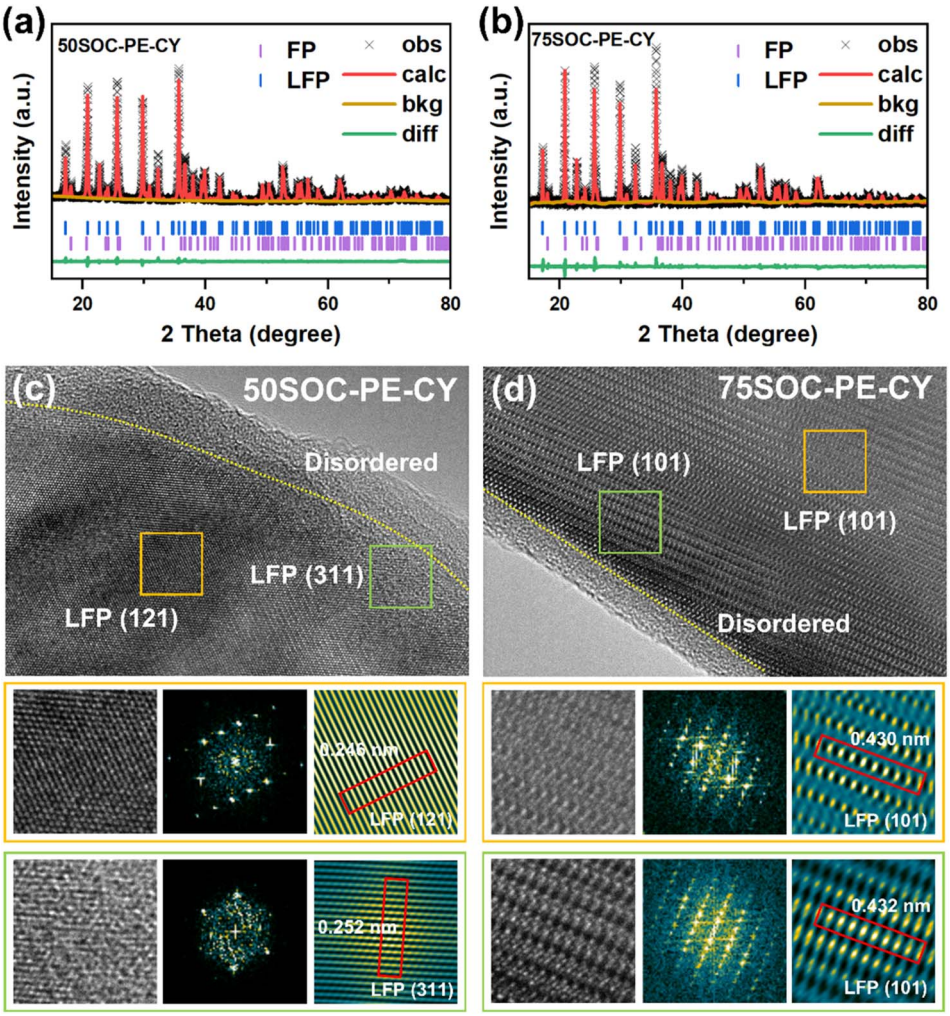

Fig. 7 Structural evolution and characterization of powder microstructure during long-term high-temperature storage. XRD Rietveld refinement results of cathode powders from (a) 50SOC-PE-CY, (b) 75SOC-PE-CY. HRTEM images and the corresponding FFT/iFFT images of (c) 50SOC-PE-CY, (d) 75SOC-PE-CY.

cathode, influencing the extent of phase transformation and lithium reversibility during long-term operation.

To further investigate the structural evolution of the negative electrode following long-term storage and subsequent cycling, X-ray diffraction (XRD) and Raman spectroscopy were employed, as presented in Fig. 8. Fig. 8a shows the XRD patterns of graphite electrodes extracted from cells stored under different SOC conditions at 55 °C. The (002) diffraction peak of the graphite in the 75SOC-NE-CY cell shifts toward a higher angle relative to the 50SOC-NE-CY sample, indicating a decrease in interlayer spacing. Since lithium-ion intercalation kinetics are strongly dependent on graphite's interlayer distance, this contraction implies hindered Li^+ diffusion and less efficient insertion/extraction during cycling. Such structural compaction is likely driven by accumulated thermal and mechanical stress during storage at high SOC, which may also contribute to particle-level damage. Raman spectroscopy was used to further evaluate structural disorder and changes in the graphite lattice, as shown in Fig. 8b. The spectra display three characteristic bands: the D band at ~1350 cm^{-1} (indicative of lattice defects), the G band at ~1580 cm^{-1} (reflecting sp^2-bonded carbon structures), and the G′ band near 2700 cm^{-1} (related to interlayer stacking order). The intensity ratio of the D to G bands (I_D/I_G), a widely used indicator of defect concentration, increases significantly in the 75SOC-NE-CY compared to the 50SOC-NE-CY. This elevation in I_D/I_G suggests a higher density of structural defects, which likely results from enhanced surface reactions, Li^+ trapping, or SEI thickening during high-SOC storage. Notably, these structural variations persist into the cycling phase, indicating that damage incurred during storage may compromise subsequent electrochemical behavior. The observed differences between the two SOC conditions suggest that calendar aging, particularly under elevated SOC and temperature, plays a critical role in shaping the mechanical and structural state of the anode prior to cycling. HRTEM images (Fig. S11†) reveal that the graphite anode stored at 50% SOC maintains well-defined and continuous lattice fringes, indicating relatively stable structural integrity and more stable interfacial conditions. In contrast, storage at 75% SOC induces localized interfacial inhomogeneity, lattice distortion, and an

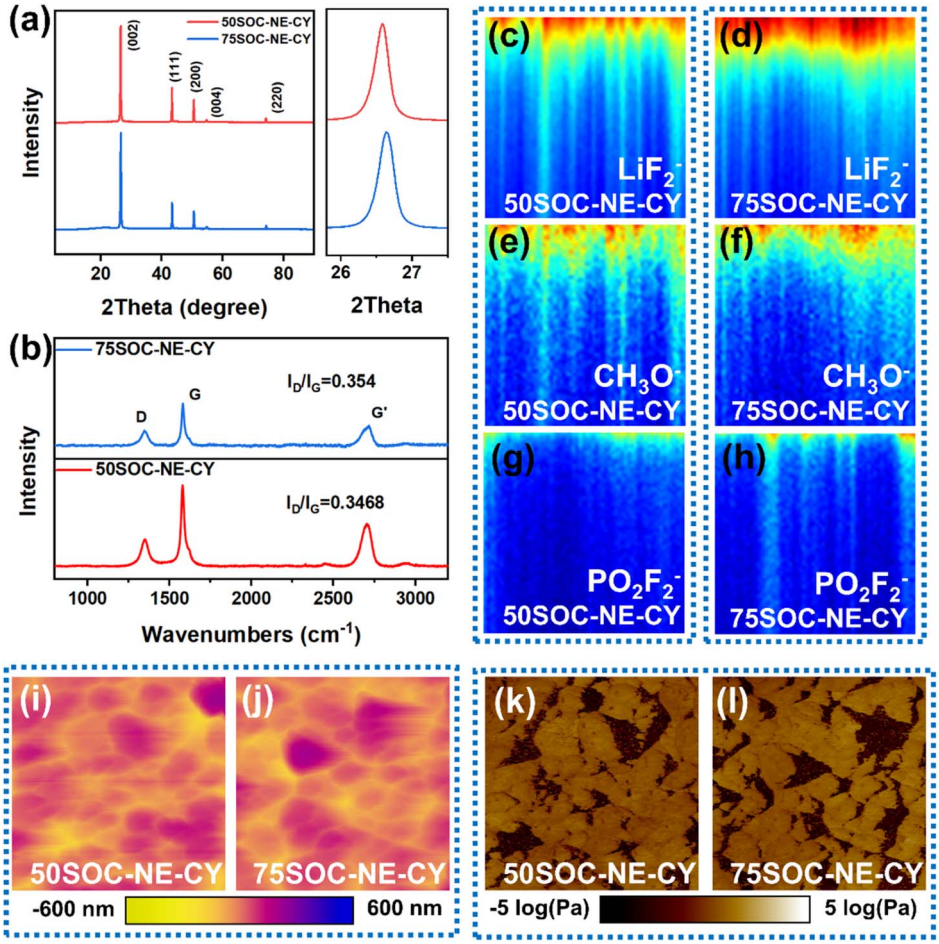

Fig. 8 Surface composition analysis and characterization of negative electrodes after cycling. (a) XRD patterns and (b) Raman spectra of negative electrode from 50SOC-NE-CY and 75SOC-NE-CY. ToF-SIMS of (c, e and g) 50SOC-NE-CY, (d, f and h) 75SOC-NE-CY. Height images of (i) 50SOC-NE-CY, (j) 75SOC-NE-CY. Modulus images of (k) 50SOC-NE-CY, (l) 75SOC-NE-CY.

early onset of SEI accumulation. Upon subsequent prolonged cycling, the SOC-dependent differences become increasingly prominent. The SEI layer on the 50% SOC samples remains relatively thin, uniform, and primarily amorphous, while the 75% SOC samples exhibit significantly thicker and more heterogeneous SEI layers. Furthermore, a gradual expansion of the graphite *d*(002) interlayer spacing under high SOC conditions indicates increasing lattice disorder and reduced graphitization, highlighting aggravated structural degradation alongside intensified interfacial side reactions. These results collectively demonstrate that high SOC storage accelerates both interfacial and bulk structural deterioration, while lower SOC storage effectively mitigates such degradation pathways and supports longer-term electrochemical stability.

To examine the structural evolution of the solid electrolyte interphase (SEI) layer on the graphite anode after long-term cycling under varying storage conditions, Time-of-Flight Secondary Ion Mass Spectrometry (ToF-SIMS) and Atomic Force Microscopy (AFM) were employed. ToF-SIMS analysis was used to identify the compositional changes in surface species, revealing fragments such as $PO_2F_2^-$—a decomposition product of $LiPF_6$—CHO^- from organic electrolyte reduction, and LiF_2^-, which is associated with the accumulation of electronically isolated ("dead") lithium.[41,45] At 55 °C, the graphite anode from the cell previously stored at 50% SOC showed significantly fewer side reaction products than that from the 75% SOC-stored counterpart. The increase in fragment intensity on the 75SOC electrode surface indicates a greater extent of SEI degradation and parasitic reactions during cycling, mirroring trends observed at the cathode interface. To further explore changes in surface morphology and mechanical properties, AFM was conducted to measure topographical roughness and map the Young's modulus distribution. As shown in Fig. 8i–l, with increasing SOC, the anode surface became progressively rougher, indicating non-uniform SEI formation and accumulation. In particular, the 75SOC-NE-CY sample exhibited not only elevated roughness but also a substantially broader modulus distribution compared to the 50SOC-NE-CY electrode. This heterogeneity arises from the concurrent development of high-modulus inorganic lithium salt residues and low-modulus organic electrolyte decomposition products, pointing to a dual-pathway degradation mechanism. The coexistence of these contrasting mechanical domains suggests that elevated SOC during storage enhances chemical instability at the electrode–

electrolyte interface, leading to the formation of a mechanically and chemically heterogeneous SEI. These observations underscore the pronounced sensitivity of SEI composition and morphology to pre-cycling storage conditions, particularly SOC, and reflect the extended influence of calendar aging on interfacial stability during subsequent cycling.

Recent research across various battery chemistries has underscored the fundamental importance of interfacial and structural regulation in mitigating long-term degradation and ensuring electrochemical stability during storage.[46–50] Our study confirms that prolonged storage at high state-of-charge (SOC) significantly accelerates electrolyte decomposition, SEI/CEI thickening, and mechanical deterioration of electrode materials, resulting in lithium inventory loss, increased impedance, and compromised cycling performance. Calendar aging should thus be recognized as an active preconditioning process that shapes the long-term aging trajectory. To mitigate these effects, we propose several strategies: avoid extended high-SOC storage, maintain moderate SOC levels (40–60%) during idle periods, employ intelligent BMS capable of adaptive SOC management based on real-time diagnostics, and conduct periodic shallow cycling or reconditioning protocols to preserve interfacial stability. These insights may guide future optimization of storage protocols and battery management strategies to prolong service life under diverse application scenarios.

Conclusions

This study systematically investigated the calendar aging behavior of $LiFePO_4$/graphite pouch cells stored at 55 °C for one year under two different SOC conditions (50% and 75%), and further evaluated their impact on subsequent cycling performance. The results reveal that higher SOC storage induces more pronounced capacity fade, increased interfacial resistance, and aggravated structural and chemical degradation, particularly on the graphite anode side. Comprehensive characterizations including XRD, Raman spectroscopy, SEM, HRTEM, ToF-SIMS, XPS, and AFM demonstrate that high SOC accelerates interlayer contraction of graphite, intensifies SEI layer growth, and promotes the accumulation of LiF and organic lithium salts. These changes hinder lithium-ion transport, reduce structural reversibility, and impair long-term cycling stability. *In situ* XRD results show that both cathode and anode materials exhibit altered phase transition behavior after storage, with graphite exhibiting stronger lattice evolution under higher SOC. Meanwhile, surface roughness and modulus distribution analyses further confirm the formation of unstable and heterogeneous SEI layers after prolonged high-SOC storage. Notably, although the crystalline structure of LFP remains largely intact, interfacial changes and mechanical fatigue driven by SOC-dependent storage significantly influence the degradation kinetics during later cycling. These findings underscore the coupled nature of calendar and cycle aging and highlight the importance of managing SOC during storage. Unlike studies that examine calendar and cycling aging independently, this work establishes a mechanistic link between the two, demonstrating how prior calendar aging dictates subsequent failure modes. This insight is particularly relevant for long-term applications such as grid storage or electric vehicle standby phases. Moving forward, future efforts should focus on designing integrated aging protocols that consider both storage and usage conditions, as well as developing interfacial stabilizers or adaptive charging strategies that mitigate calendar aging effects and preserve performance over extended service life.

Data availability

The DRT analysis software used in this study was developed by the research group of Francesco Ciucci, and is available for download at [**https://github.com/ciuccislab**]. The software for Gsas1 can be found at [**https://subversion.xray.aps.anl.gov/trac/EXPGUI**].

Author contributions

Wenjun Shen: writing – original draft, methodology, data curation, conceptualization. Jinyang Dong: writing – visualization, software, methodology. Yun Lu: methodology, investigation. Kang Yan: methodology, investigation. Yibiao Guan: methodology, investigation. Guangjin Zhao: methodology, investigation. Bowen Li: methodology, investigation. Xi Wang: methodology, investigation. Rui Tang: methodology, investigation. Jialong Zhou: methodology, investigation. Ning Li: methodology, investigation. Yuefeng Su: writing – review & editing, supervision, resources, project administration. Feng Wu: resources, funding acquisition, conceptualization. Lai Chen: writing – review & editing, supervision, resources, project administration.

Conflicts of interest

There are no conflicts to declare.

Acknowledgements

This work was supported by the National Key R&D Program of China (2021YFB2401800). L. Chen acknowledges the support from Beijing Nova Program (20230484241). J. Y. Dong acknowledges the support from the China Postdoctoral Science Foundation (2024M754084) and the Postdoctoral Fellowship Program of CPSF (GZB20230931). The authors also thank for the support from Initial Energy Science & Technology Co., Ltd (IEST).

References

1 T. Kim, W. Song, D.-Y. Son, L. K. Ono and Y. Qi, *J. Mater. Chem. A*, 2019, **7**, 2942–2964.
2 X. Hu, L. Xu, X. Lin and M. Pecht, *Joule*, 2020, **4**, 310–346.
3 Y. Che, X. Hu, X. Lin, J. Guo and R. Teodorescu, *Energy Environ. Sci.*, 2023, **16**, 338–371.
4 R. Li, N. D. Kirkaldy, F. F. Oehler, M. Marinescu, G. J. Offer and S. E. O'Kane, *Nat. Commun.*, 2025, **16**, 2776.

5 Y. Jia, X. Gao, L. Ma and J. Xu, *Adv. Energy Mater.*, 2023, **13**, 2300368.
6 H. Zhang, Y. Peng, Y. Hu, S. Pan, S. Tang, Y. Luo, Y. Liang, Y. Liao, Y. Lin and K. Zhang, *Adv. Energy Mater.*, 2025, 2404997.
7 A. Geslin, L. Xu, D. Ganapathi, K. Moy, W. C. Chueh and S. Onori, *Nat. Energy*, 2025, **10**, 172–180.
8 Y. Peng, C. Zhong, M. Ding, H. Zhang, Y. Jin, Y. Hu, Y. Liao, L. Yang, S. Wang and X. Yin, *Adv. Funct. Mater.*, 2024, **34**, 2404495.
9 G. Li, *Adv. Energy Mater.*, 2021, **11**, 2002891.
10 F. J. Méndez-Corbacho, D. Nieto-Castro, I. Moreno-Artabe, D. del Olmo, G. Baraldi and E. Ayerbe, *ChemElectroChem*, 2024, **11**, e202300830.
11 D. Yin, J. Ni, X. Shi, H. Liu, M. Lv, W. Shen and G. Zhang, *ACS Appl. Energy Mater.*, 2025, **8**, 3491–3499.
12 S. Kim, P. Barnes, H. Zhang, C. Efaw, Y. Wang, B. Park, B. Li, B.-R. Chen, M. C. Evans and B. Liaw, *Energy Storage Mater.*, 2024, **65**, 103147.
13 L. Wang, J. Qiu, X. Wang, L. Chen, G. Cao, J. Wang, H. Zhang and X. He, *EScience*, 2022, **2**, 125–137.
14 J.-H. Hyun, M.-J. Yi, H. Jung, S.-H. Lee, J. H. Um and S.-H. Yu, *Energy Storage Mater.*, 2023, **54**, 146–155.
15 E. J. Dufek, T. R. Tanim, B.-R. Chen and S. Kim, *Joule*, 2022, **6**, 1363–1367.
16 Y. Liao, H. Zhang, Y. Peng, Y. Hu, J. Liang, Z. Gong, Y. Wei and Y. Yang, *Adv. Energy Mater.*, 2024, **14**, 2304295.
17 Y. Zhu, J. Zhu, B. Jiang, X. Wang, X. Wei and H. Dai, *J. Energy Storage*, 2023, **60**, 106624.
18 H. Hyun, H. Yoon, S. Choi, J. Kim, S. Y. Kim, T. Regier, Z. Arthur, S. Kim and J. Lim, *Energy Environ. Sci.*, 2023, **16**, 3968–3983.
19 C. Fang, J. Li, M. Zhang, Y. Zhang, F. Yang, J. Z. Lee, M.-H. Lee, J. Alvarado, M. A. Schroeder and Y. Yang, *Nature*, 2019, **572**, 511–515.
20 P. Nakhanivej, H. H. Rana, H. Kim, B. Y. Xia and H. S. Park, *ACS Nano*, 2020, **14**, 7696–7703.
21 J. Zhu, M. Knapp, D. R. Sørensen, M. Heere, M. S. Darma, M. Müller, L. Mereacre, H. Dai, A. Senyshyn and X. Wei, *J. Power Sources*, 2021, **489**, 229422.
22 W. Kim, C. Hwang, Y. M. Kim, J.-S. Yu, Y.-J. Kim, K. J. Kim and H.-s. Kim, *J. Mater. Chem. A*, 2024, **12**, 14786–14791.
23 L. Yang, Y. Tian, J. Chen, J. Gao, Z. Long, W. Deng, G. Zou, H. Hou and X. Ji, *J. Mater. Chem. A*, 2021, **9**, 24686–24694.
24 S. Sun, T. Guan, X. Cheng, P. Zuo, Y. Gao, C. Du and G. Yin, *RSC Adv.*, 2018, **8**, 25695–25703.
25 S. Oh, A. R. Jeon, G. Lim, M. K. Cho, K. H. Chae, S. S. Sohn, M. Lee, S.-K. Jung and J. Hong, *Energy Storage Mater.*, 2024, **65**, 103169.
26 K. Sun, X. Li, K. Fu, H. Yang, L. Gong and P. Tan, *Mater. Today Commun.*, 2024, **39**, 108765.
27 V. N. Lam, X. Cui, F. Stroebl, M. Uppaluri, S. Onori and W. C. Chueh, *Joule*, 2025, **9**, 101796.
28 D. Li, D. L. Danilov, J. Xie, L. Raijmakers, L. Gao, Y. Yang and P. H. L. Notten, *Electrochim. Acta*, 2016, **190**, 1124–1133.
29 M. Naumann, M. Schimpe, P. Keil, H. C. Hesse and A. Jossen, *J. Energy Storage*, 2018, **17**, 153–169.
30 O. S. Mendoza-Hernandez, E. Hosono, D. Asakura, H. Matsuda, S. Shironita, M. Umeda and Y. Sone, *J. Electrochem. Soc.*, 2019, **166**, A3525–A3530.
31 Y. Peng, M. Ding, K. Zhang, H. Zhang, Y. Hu, Y. Lin, W. Hu, Y. Liao, S. Tang, J. Liang, Y. Wei, Z. Gong, Y. Jin and Y. Yang, *ACS Energy Lett.*, 2024, **9**, 6022–6028.
32 M. Bozorgchenani, G. Kucinskis, M. Wohlfahrt-Mehrens and T. Waldmann, *J. Electrochem. Soc.*, 2022, **169**, 030509.
33 J. Zhu, M. Knapp, X. Liu, P. Yan, H. Dai, X. Wei and H. Ehrenberg, *IEEE Trans. Transp. Electrif.*, 2020, **7**, 410–421.
34 R. Tang, J. Dong, C. Wang, Y. Guan, A. Yin, K. Yan, Y. Lu, N. Li, G. Zhao and B. Li, *Adv. Funct. Mater.*, 2025, 2421284.
35 R. Li, L. Bao, L. Chen, C. Zha, J. Dong, N. Qi, R. Tang, Y. Lu, M. Wang and R. Huang, *Sci. Bull.*, 2023, **68**, 3055–3079.
36 X. Qiao, Y. Mu, J. Peng, B. Pei and S. Wang, *ACS Appl. Energy Mater.*, 2025, **8**, 2209–2218.
37 Z. Li, Y. X. Yao, M. Zheng, S. Sun, Y. Yang, Y. Xiao, L. Xu, C. B. Jin, X. Y. Yue and T. Song, *Angew. Chem.*, 2025, **137**, e202409409.
38 W. Shi, L. Liu, R. Xu, R. Sun, J. Dong and X. Kang, *Energy Storage Mater.*, 2025, **76**, 104143.
39 D. Zhao, J. Chen, M. Tao, M. Su, W. Huang, P. Shan, H. Lin, Y. Zhou, Z. He and Y. Jin, *Energy Storage Mater.*, 2025, **75**, 104057.
40 W. Wu, Y. Lin, Y. Hu, Z. He and Y. Yang, *J. Energy Chem.*, 2024, **171**, 010510.
41 X. X. Zhao, X. T. Wang, J. Z. Guo, Z. Y. Gu, J. M. Cao, J. L. Yang, F. Q. Lu, J. P. Zhang and X. L. Wu, *Adv. Mater.*, 2024, **36**, 2308927.
42 M. Fan, Q. Meng, X. Chang, C. F. Gu, X. H. Meng, Y. X. Yin, H. Li, L. J. Wan and Y. G. Guo, *Adv. Energy Mater.*, 2022, **12**, 2103630.
43 J. D. McBrayer, M.-T. F. Rodrigues, M. C. Schulze, D. P. Abraham, C. A. Apblett, I. Bloom, G. M. Carroll, A. M. Colclasure, C. Fang and K. L. Harrison, *Nat. Energy*, 2021, **6**, 866–872.
44 W. Zhao, K. Wang, X. Fan, F. Ren, X. Xu, Y. Liu, S. Xiong, X. Liu, Z. Zhang and M. Si, *Angew. Chem.*, 2023, **135**, e202305281.
45 Z. Shi, Y. Wang, X. Yue, J. Zhao, M. Fang, J. Liu, Y. Chen, Y. Dong, X. Yan and Z. Liang, *Adv. Mater.*, 2024, **36**, 2401711.
46 C. Liu, Y. Zhu, S. Di, J. He, P. Niu, A. Kelarakis, M. Krysmann, S. Wang and L. Li, *Electron*, 2024, **2**, e29.
47 P. Liang, S. Di, Y. Zhu, Z. Li, S. Wang and L. Li, *Angew. Chem.*, 2024, **136**, e202409871.
48 S. Di, H. Li, B. Zhai, X. Zhi, P. Niu, S. Wang and L. Li, *Proc. Natl. Acad. Sci. U. S. A.*, 2023, **120**, e2302375120.
49 W. Yan, J. Xian, S. Zhang, J. Zhang, K. Liu, J. L. Yang, F. Tao, R. Liu, Q. Liu and P. Yang, *Adv. Sci.*, 2025, 2502834.
50 X. Tan, Z. Chen, T. Liu, Y. Zhang, M. Zhang, S. Li, W. Chu, K. Liu, P. Yang and F. Pan, *Adv. Mater.*, 2023, **35**, 2301096.